

Experimental study of particle trajectories below deep-water surface gravity wave groups

T. S. van den Bremer^a, C. Whittaker^b, R. Calvert^a, A. Raby^c and P. H. Taylor^d

^aDepartment of Engineering Science, University of Oxford, Oxford OX1 3PJ, UK

^bDepartment of Civil and Environmental Engineering, University of Auckland, Auckland 1010, New Zealand

^cSchool of Engineering, University of Plymouth, Plymouth PL4 8AA, UK

^dFaculty of Engineering and Mathematical Sciences, University of Western Australia, Crawley WA 6009, Australia

(Received xx; revised xx; accepted xx)

Due to the interplay between the forward Stokes drift and the backward wave-induced Eulerian return flow, Lagrangian particles underneath surface gravity wave groups can follow different trajectories depending on their initial depth below the surface. The motion of particles near the free surface is dominated by the waves and their Stokes drift, whereas particles at large depths follow horseshoe-shaped trajectories dominated by the Eulerian return flow. For unidirectional wave groups, a small net displacement in the direction of travel of the group results near the surface, and is accompanied by a net particle displacement in the opposite direction at depth. For deep-water waves, we study these trajectories experimentally by means of Particle Tracking Velocimetry in a two-dimensional flume. In doing so, we provide visual illustration of Lagrangian trajectories under groups, including the contributions of both the Stokes drift and the Eulerian return flow to both the horizontal and the vertical Lagrangian displacements. We compare our experimental results to leading-order solutions of the irrotational water wave equations, finding good agreement.

1. Introduction

The oscillatory motion of Lagrangian particles below surface gravity waves is subject to a net drift in the direction of wave propagation known as Stokes drift (Stokes 1847). For wave groups, the net positive transport associated with the Stokes drift becomes divergent on the group scale and is accompanied by an opposing Eulerian return flow (Longuet-Higgins & Stewart 1962). The total Lagrangian velocity is given by the sum of the Stokes drift and the induced Eulerian flow, and the resulting particle trajectories and displacements have been examined theoretically by van den Bremer & Taylor (2015, 2016).

In the ocean, Stokes drift can provide a significant contribution to the trajectories of drifters (Röhrs *et al.* 2012) and must be accounted for in search and recovery missions such as the search for debris from the presumed location of the 2014 MH370 airplane crash (Trinanes *et al.* 2016). Stokes drift can be important in the local modelling of oil spills (Christensen & Terrile 2009; Drivdal *et al.* 2014; Jones *et al.* 2016). In the near-surface transport and dispersion of plastic pollution, Stokes drift plays a potentially important yet largely unexplored role (e.g. Lebreton *et al.* (2018)). Furthermore, Stokes drift is considered a mechanism driving global ocean circulation (McWilliams & Restrepo 1999; Belcher *et al.* 2012), Langmuir turbulence (Craik & Leibovich 1976; D’Asaro *et al.* 2014; Sullivan & McWilliams 2010) and sub-mesoscale ocean instability (Haney *et al.* 2015; McWilliams 2016).

Experimentally, many authors have considered Stokes drift in laboratory wave flumes. As a visual illustration, Wallet & Ruellan’s (1950) seminal image of orbits that do not quite close is

reproduced in van Dyke's (1982) *Album of Fluid Motion*. Yet, there remains some confusion in the literature whether a net drift should be observed (see the discussion in Monismith *et al.* (2007), Weber (2011), Grue & Kolaas (2017), van den Bremer & Breivik (2017) and Deike *et al.* (2017)). To explain this, three effects must be taken into account: boundary layers, the origin of vorticity in the interior of the fluid and breaking.

Longuet-Higgins (1953) showed the mass-transport velocity can be significantly different from the irrotational theory of Stokes (1847), with additional net transport arising in the oscillating bottom and surface boundary layers. Explaining experiments by Bagnold (1947), Longuet-Higgins (1953) showed the Lagrangian transport in the boundary layers is positive and does not disappear in the limit of infinite Reynolds number. This boundary layer streaming has recently been studied for very steep waves by Grue & Kolaas (2017), who observed significant additional streaming and associated shear in both the bottom and free surface boundary layers, more than can be predicted by the boundary layer streaming solution of Longuet-Higgins (1953), which Grue & Kolaas (2017) noted may be invalid due to the large steepness of the waves.

For periodic waves, which are the focus of almost all experimental studies focussing on wave-induced mean flows, the net depth-integrated mass flux must be zero in a closed flume. The Stokes transport must be accompanied by a Eulerian return current driven by a setup in the direction downstream of wave propagation, which is conceptually distinct from the return flow forced by the packet structure examined herein. This closed-flume return flow is irrotational, unless vorticity can be transported into the interior of the fluid. Longuet-Higgins (1953) derived two classes of analytical solutions for this vorticity transport: a 'conduction' solution and a 'convection' solution. Depending on the ratio of the wave amplitude a to the thickness of the boundary layer δ , the transport of vorticity takes place by viscous 'conduction' (a^2/δ^2 small) from the bottom and free surface boundary layers, or convection with the mass-transport velocity (a^2/δ^2 large), from the wavemaker or the beach at the other end, where vorticity can be generated. If one considers a motion that is started from rest, the motion in the interior of the fluid will always be initially irrotational, and it will take considerable time for vorticity to be advected or diffused from the vertical or horizontal boundaries, respectively. Finally, as also pointed out by Longuet-Higgins (1953), the convection solution may not be stable.

In the conduction regime, Groeneweg & Klopman (1998) compare their more generally applicable generalized Lagrangian mean model for wave-current interaction to the conduction solution of Longuet-Higgins (1953), showing near perfect agreement, and to the laboratory measurements in a very shallow and long closed flume by Mei *et al.* (1972), finding good agreement for intermediate water depth ($kh = 1.0$), but less good agreement for deeper water ($kh = 1.8$). However, most experimental studies are in the convection regime. Swan (1990) demonstrated that convection indeed plays an important part within a relatively deep experimental wave flume: vorticity generated at the end conditions is convected backwards with the mass transport velocity and the near-shore region progressively influences the entire length of the wave flume, although the flow field is not always stable. By installing a plastic sheet at the toe of the beach, Swan & Sleath (1990) could obtain long-time stable conditions that agreed better with their 4th-order finite-depth extension of the irrotational solution for Lagrangian transport in a closed domain. Umeyama (2012) performed a similar expansion, but focused explicitly on particle trajectories and found reasonable agreement with experimentally obtained trajectories. Paprota *et al.* (2016), who took their measurements after a relatively short wave train of periodic waves in a relatively long flume, found good agreement with the irrotational theory of Stokes (1847), supplemented by a closed-flume return current. For waves of intermediate water depth ($kh = O(1)$) and very large steepness, Grue & Kolaas (2017) found good agreement with nonlinear irrotational theory in the interior of the fluid in a set of very high-quality experiments. Their experiments were stopped long before the first waves reach the end of their open-ended flume, but the length of their wave train remains long relative to the water depth. Based on their experiments, Monismith

et al. (2007) have suggested a cancellation of the Stokes drift by a Eulerian mean flow that is equal and opposite at every depth. Their experiment were done in the presence of a pre-existing sheared current in a recirculating flume, which could help explain their observation. The current could also advect vorticity at a faster rate than the wave-induced mean flow.

If the waves are breaking, transport of Lagrangian particles near the surface will be considerably enhanced, as observed experimentally by Melville & Rapp (1988) and recently explained using numerical simulations and a scaling argument for breaking by Deike *et al.* (2017) with implications for surfing (Pizzo 2017). Breaking also has the capacity to transport vorticity into the interior of the fluid (Pizzo & Melville 2013).

This paper presents an experimental study of Lagrangian trajectories and transport by unidirectional, deep-water, small-amplitude, short-length yet quasi-monochromatic surface gravity wave groups. In doing so, we visualize experimentally for the first time the wave-induced Eulerian return flow for groups. We also show that our experimental observations in this regime are in good agreement with leading-order solutions to the irrotational water wave equations. Our experiments using short-length groups in an otherwise quiescent flume have the advantage of not generating a closed-flume return flow, which may transport vorticity, is potentially unstable, and difficult to control experimentally.

Furthermore, our experiments demonstrate the existence of a vertical component to the Stokes drift, which only exists for wave groups and results in a positive (temporary) vertical particle displacement underneath the centre of the group. This positive vertical displacement by the Stokes drift has been predicted by Herbers & Janssen (2016), who showed the set-down of the wave-averaged free surface in Eulerian records can appear as (significant) set-up in Lagrangian (buoy) records. Nevertheless, a vertical component to the Stokes drift (for groups) has been contentious in adaptations of the work by Craik & Leibovich (1976) in the context of ocean circulation and Langmuir circulation. McWilliams *et al.* (2004) noted that the vertical Stokes drift is zero and introduced a vertically-divergent vertical pseudo-velocity to compensate for the horizontal divergence of the Stokes drift. Although Mellor (2016) allows for a horizontally-divergent Stokes drift, he still requires the vertical Stokes drift component to be zero. We emphasize that the Stokes drift velocity is generally divergent for groups; this is consistent with generalized Lagrangian-mean theory (Andrews & McIntyre 1978), as shown by McIntyre (1988). Accordingly, a vertical Stokes drift component arises for groups, as can be easily derived for irrotational surface gravity waves and is confirmed experimentally herein.

This paper is laid out as follows. First, §2 briefly summarizes the irrotational solutions for wave groups, followed by a description of our experimental methodology in §3. We present results in §4, including illustrations of the Lagrangian orbits, a comparison with irrotational water wave theory and an assessment of the experimental error, and draw conclusions in §5.

2. Irrotational water wave theory for wave groups

2.1. Governing equations and leading-order solutions

In a two-dimensional body of water of depth d with coordinate system (x, z) and z the vertical coordinate measured from the undisturbed water level upwards, inviscid, incompressible and irrotational flow leads to Laplace $\nabla^2\phi = 0$ for $-d \leq z \leq \eta(x, t)$ as the governing equation, where the velocity vector $\mathbf{u} = \nabla\phi$ and $\eta(x, t)$ denotes the free surface. By retaining terms up to quadratic in the amplitude of the waves, the kinematic free surface boundary condition ($w - \partial\eta/\partial t - u\partial\eta/\partial x = 0$) and the dynamic free surface boundary condition ($g\eta + \partial\phi/\partial t + (u^2 + w^2)/2 = 0$), both at $z = \eta(x, t)$, can be combined into two forcing equations for the mean flow and the wave-averaged free surface, respectively (e.g. Longuet-Higgins & Stewart (1964); McAllister *et al.*

(2018)):

$$\left(\frac{\partial}{\partial z} + \frac{1}{g} \frac{\partial^2}{\partial t^2} \right) \phi^{(2)} \Big|_{z=0} = \overline{\frac{\partial}{\partial x} (u^{(1)}|_{z=0} \eta^{(1)})} + O(\alpha^2 \epsilon^3), \quad \eta^{(2)} = \frac{-1}{g} \frac{\partial \phi^{(2)}}{\partial t} \Big|_{z=0} + O(\alpha^2 \epsilon^3), \quad (2.1a,b)$$

where the superscripts denote the order in amplitude, and we only retain wave-averaged terms here, as indicated by the overlines on the right-hand side of (2.1a). The small parameter corresponding to amplitude, steepness, is denoted by $\alpha \equiv k_0 |a_0|$, where a_0 is the typical amplitude of the surface elevation and k_0 the wavenumber of the carrier wave. Explicitly, we thus have for the Stokes expansion in α that $\phi = \phi^{(1)} + \phi^{(2)} + O(\alpha^3)$ and $\eta = \eta^{(1)} + \eta^{(2)} + O(\alpha^3)$, where we will only retain the wave-averaged terms in $\phi^{(2)}$ and $\eta^{(2)}$. In (2.1) we have made the additional assumption that $k_0 d \gg 1$, so that the set-down of the wave-averaged free surface $\eta^{(2)}$ does not directly affect the mean flow (McIntyre 1981; McAllister *et al.* 2018). More specifically, we set $\eta^{(1)} = \text{Re}[A_0(X) \exp(\iota(k_0 x - \omega_0 t)) + \epsilon A_1(X) \exp(\iota(k_0 x - \omega_0 t))]$ and $\phi^{(1)} = \text{Re}[B_0 \exp(k_0 z + \iota(k_0 x - \omega_0 t)) + \epsilon B_1 \exp(k_0 z + \iota(k_0 x - \omega_0 t))]$, where $X \equiv \epsilon(x - c_{g,0} t)$ with $\epsilon \equiv 1/(k_0 \sigma)$, σ the characteristic length of the group and $c_{g,0} = d\omega_0/dk_0 = \omega_0/(2k_0)$ the group velocity. The linear ($O(\alpha)$) polarization relationships at the zeroth and first order in ϵ are given in table 1.

Our focus is on leading-order terms; we ignore dispersion of the group (e.g. van den Bremer & Taylor (2016)), and the second-order equations in steepness (2.1) are accurate up to $O(\epsilon^3)$ in the bandwidth parameter ϵ , as can be shown from the linear polarization relationships in table 1. The leading-order, non-dispersive mean flow solution is given by combining the linear polarization relationships in table 1 and solving Laplace $\nabla^2 \phi^{(2)} = 0$ subject to the bottom boundary condition $\partial \phi^{(2)}/\partial z = 0$ at $z = -d$ and the surface forcing (2.1a) (see also van den Bremer & Taylor (2016))

$$\phi_E^{(2)} = \frac{-\omega_0}{4\pi} \int_{-\infty}^{\infty} \frac{\cosh(|\omega|(z+d)/c_{g,0})}{\sinh(|\omega|d/c_{g,0})} \frac{\omega}{|\omega|} \frac{\widehat{\iota|A_0|^2}}{1 - \frac{\omega^2 c_{g,0}}{g|\omega| \tanh(|\omega|d/c_{g,0})}} \exp(i\omega \tilde{t}) d\omega, \quad (2.2)$$

where we choose $c_{g,0} > 0$ and define $\tilde{t} \equiv t - x/c_{g,0}$. We have expressed the solution as an inverse Fourier transform in time to enable evaluation of the Fourier transform of the square of the leading-order packet $\widehat{|A_0|^2}$ directly from point measurements of the surface elevation. It is instructive to consider the shallow return flow limit $d/\sigma \ll 1$, in which case the velocity field corresponding to (2.2) becomes more simply

$$u_E^{(2)} = -\frac{\omega_0}{2d} \frac{1}{1 - 1/(4k_0 d)} |A_0|^2 \quad \text{and} \quad w_E^{(2)} = -\frac{k_0}{1 - 1/(4k_0 d)} \frac{d+z}{d} \partial_{\tilde{t}} |A_0|^2, \quad (2.3a,b)$$

where $1/(4k_0 d)$ in the denominator will be small as $k_0 d \gg 1$.

The mean motion of the Lagrangian particles we examine is determined by the sum of the Stokes drift \mathbf{u}_s and the wave-induced Eulerian mean flow \mathbf{u}_E : $\mathbf{u}_L = \mathbf{u}_s + \mathbf{u}_E$ (e.g. Bühler (2014)). The Stokes drift can be determined from the linear waves using the linear polarization relationships in table 1:

$$\mathbf{u}_s \equiv \overline{\boldsymbol{\xi}^{(1)} \cdot \nabla \mathbf{u}^{(1)}} = k_0 \left(\omega_0, \frac{3}{2} \frac{\partial}{\partial \tilde{t}} \right) |A_0|^2 \exp(2k_0 z), \quad (2.4)$$

where $\mathbf{u}^{(1)}$ is the velocity field of the linear wave and $\boldsymbol{\xi}^{(1)}$ the corresponding linear displacement vector with components $\boldsymbol{\xi}^{(1)} = (\xi_x^{(1)}, \xi_z^{(1)})$, which can be evaluated from the linear velocity field according to $\partial \boldsymbol{\xi}^{(1)}/\partial t = \mathbf{u}^{(1)}$. For groups, it is evident from (2.4) that a non-zero vertical Stokes drift exists. Like their horizontal components, the vertical velocities of the return flow and Stokes drift are of opposite sign. Finally, we note that the Stokes drift velocity field is divergent, and (2.4) satisfies the identity for volume conservation $\nabla \cdot \mathbf{u}_s = (1/2) \partial_{tzz} (\overline{\eta^{(1)}}^2)$ from generalized

Field	$O(1)$	$O(\varepsilon)$	Field	$O(1)$	$O(\varepsilon)$
$\xi_x^{(1)}$	ιA_0	$(\frac{1}{2} + k_0 z) \frac{1}{k_0} \varepsilon \partial_X A_0$	$\xi_z^{(1)}$	A_0	$-\iota (\frac{1}{2} + k_0 z) \frac{1}{k_0} \varepsilon \partial_X A_0$
$u^{(1)}$	$\omega_0 A_0$	$-\iota (1 + k_0 z) \frac{\omega_0}{k_0} \varepsilon \partial_X A_0$	$w^{(1)}$	$-\iota \omega_0 A_0$	$-(1 + k_0 z) \frac{\omega_0}{k_0} \varepsilon \partial_X A_0$
$\frac{\partial u^{(1)}}{\partial x}$	$\iota k_0 \omega_0 A_0$	$\omega_0 (2 + k_0 z) \varepsilon \partial_X A_0$	$\frac{\partial w^{(1)}}{\partial x}$	$k_0 \omega_0 A_0$	$-\iota \omega_0 (2 + k_0 z) \varepsilon \partial_X A_0$
$\frac{\partial u^{(1)}}{\partial z}$	$k_0 \omega_0 A_0$	$-\iota \omega_0 (2 + k_0 z) \varepsilon \partial_X A_0$	$\frac{\partial w^{(1)}}{\partial z}$	$-\iota k_0 \omega_0 A_0$	$-\omega_0 (2 + k_0 z) \varepsilon \partial_X A_0$

TABLE 1. Expressions for the different linear (in $\alpha \equiv k_0 |a_0|$) fields at $O(\alpha^1 \varepsilon^0)$ and $O(\alpha^1 \varepsilon^1)$. Values are given in terms of the leading-order amplitude envelope A_0 of the vertical displacement field. The actual fields are the real parts of the tabulated expressions after multiplication by $\exp(k_0 z + \iota \varphi_0)$, where the phase is given by $\varphi_0 = k_0 x - \omega_0 t$. We denote $\eta^{(1)} \equiv \xi_z^{(1)}(z=0)$ as the free surface.

Lagrangian-mean theory (equation (9.4) of Andrews & McIntyre (1978)), shown here correct to leading-order for our case (see also McIntyre (1988)).

2.2. Net Lagrangian displacements

After a single group has moved past, the net horizontal and the maximum vertical (positive) particle displacement arising from the Stokes drift (2.4) are given by

$$\Delta x_s \equiv \int_{-\infty}^{\infty} u_s d\tilde{t} = \omega_0 k_0 \exp(2k_0 z) \int_{-\infty}^{\infty} |A_0|^2 d\tilde{t} = 2\sqrt{\pi} \alpha^2 \sigma \exp(2k_0 z), \quad (2.5)$$

$$\Delta z_{s,\max} \equiv \int_{-\infty}^0 w_s d\tilde{t} = \frac{3\alpha^2}{2k_0} \exp(2k_0 z), \quad (2.6)$$

where $\tilde{t} = 0$ is chosen to correspond to the centre of the packet, where the maximum vertical displacement due to Stokes drift occurs. Whereas the first identity in (2.5) holds for a general packet shape, the final identity corresponds to a Gaussian packet $A_0 = a_0 \exp(-(x - c_{g,0}t)^2/2\sigma^2) = a_0 \exp(-c_{g,0}^2 \tilde{t}^2/2\sigma^2)$ for illustration.

The net horizontal and the minimum vertical (negative) particle displacement arising from the return flow (2.2) are

$$\Delta x_E \equiv \int_{-\infty}^{\infty} u_E d\tilde{t} = -\frac{1}{2} \frac{\omega_0}{d} \frac{1}{1 - 1/(4k_0 d)} \int_{-\infty}^{\infty} |A_0|^2 d\tilde{t} = -\frac{\sqrt{\pi} \alpha^2 \sigma}{k_0 d - 1/4}, \quad (2.7)$$

$$\Delta z_{E,\min} \equiv \int_{-\infty}^0 w_E d\tilde{t} = -\frac{1}{k_0} \frac{d+z}{d} \frac{\alpha^2}{1 - 1/(4k_0 d)}. \quad (2.8)$$

As for (2.5), the first identity in (2.7) holds for a general packet shape, whereas the final identity corresponds to a Gaussian packet of the form $A_0 = a_0 \exp(-(x - c_{g,0}t)^2/2\sigma^2) = a_0 \exp(-c_{g,0}^2 \tilde{t}^2/2\sigma^2)$. In §4, we evaluate the net displacements from time integration of the measured surface elevation.

We note that the net horizontal displacement does not decay with depth, in contrast to the horizontal return flow velocity (2.2) for non-shallow return flows ($d/\sigma \not\ll 1$), whereas these horizontal displacements were erroneously shown to decay with depth in van den Bremer & Taylor (2016) due to insufficiently large limits on the time integral therein for very deep water.

From (2.5-2.8), the horizontal and vertical Stokes drift and return flow displacements become

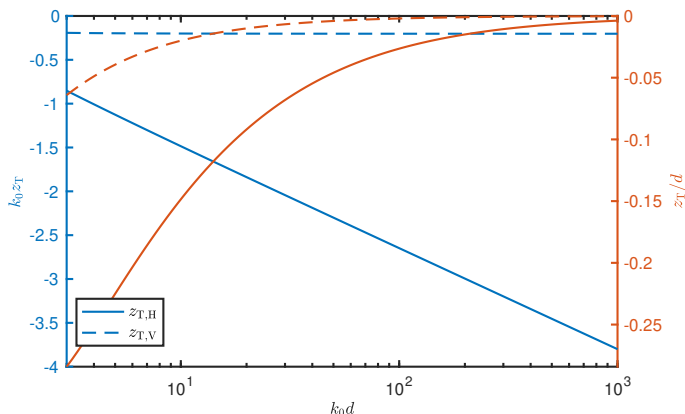


FIGURE 1. Transition depths (2.9) defined as the depths where the horizontal (continuous lines) and vertical Lagrangian (dashed lines) displacements are zero due to cancellation of their Stokes drift and Eulerian return flow components. The colours correspond to the left and right vertical axes, which are scaled differently.

equal and opposite at the respective ‘transition’ depths $z_{T,H}$ and $z_{T,V}$

$$z_{T,H} = -\frac{1}{2k_0} \log \left(2k_0 d \left(1 - \frac{1}{4k_0 d} \right) \right) \quad \text{and} \quad \frac{3}{2} \exp(2k_0 z_{T,V}) = \frac{d + z_{T,V}}{d} \frac{1}{1 - 1/(4k_0 d)} \quad (2.9a,b)$$

where $z_{T,V}$ is defined implicitly, and the horizontal transition depth (2.9a) was derived previously by van den Bremer & Taylor (2016) albeit without the small $(1 - 1/(4k_0 d))$ term to correct for the set down. Figure 1 illustrates the dependence of these transition depths on $k_0 d$. The horizontal transition depth (continuous lines) can be a significant fraction of the water depth for moderate $k_0 d$ (up to $z_{T,H}/d = -0.28$ for $k_0 d = 3$), whereas the vertical transition depth (dashed lines) is generally given by $k_0 z_{T,V} \approx -\log(3/2)/2 = -0.20$, which becomes exact in the limit $k_0 d \rightarrow \infty$. In the shallow return flow limit ($d/\sigma \ll 1$), the transition depths (2.9) also correspond to the depths below which the horizontal Lagrangian velocity becomes negative and the vertical Lagrangian velocity becomes negative (in front of the packet) or positive (behind the packet), respectively (cf. (2.3)).

3. Experimental methodology

3.1. Set-up, wave generation and data acquisition

We carried out experiments in the 35 m flume in the COAST (Coastal, Ocean and Sediment Transport) Laboratory at the University of Plymouth, UK. Our visualisation experiments are illustrated in figure 2. The flume has a width of 0.6 m and was filled to a depth $d = 0.5$ m. We used a piston-type wavemaker to generate a focused wave group with a spectral shape that linearly focuses to a Gaussian packet $A_0 = a_0 \exp(-(x_f - c_{g,0}t)^2/2\sigma^2)$ at a measurement zone located $x_f = 9.407$ m from the resting position of the wavemaker (measured free surface elevations are included in figure 9 in appendix A). Although the paddles were controlled with a combination of first- and second-order signals based on Schäffer (1996), subharmonic error waves are not expected to play a significant role for the deep-water waves examined here (Whittaker *et al.* 2017). A resistance-type wave gauge provided 128 Hz free surface elevation measurements at the focus location; the measured free surface signals provided the parameters used to predict the theoretical particle displacements for each experiment. A light-emitting diode (LED) light box located at the measurement zone (offset in the cross-flume direction from the wave gauge)

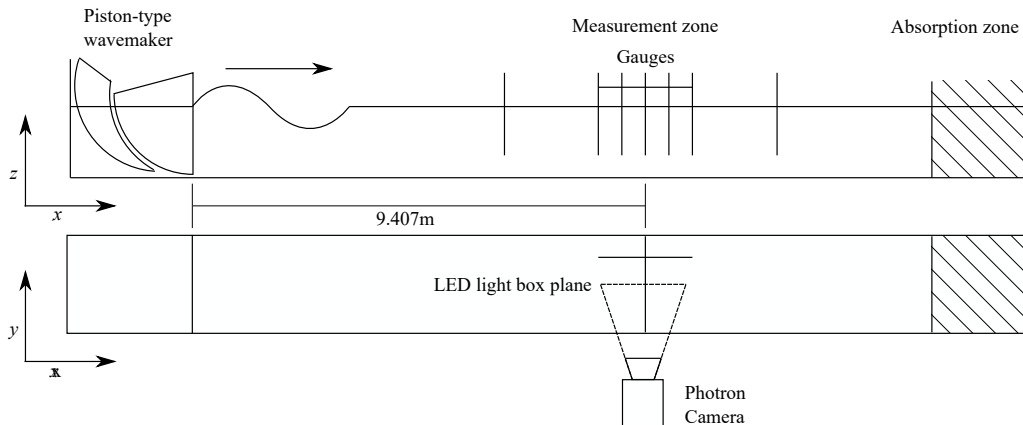


FIGURE 2. Experimental set-up used to obtain PTV measurements of trajectories below focused wave groups generated by a piston-type wavemaker in the 35 m flume in the COAST Laboratory at the University of Plymouth.

illuminated the motions of small near-neutrally buoyant particles in a plane, which were captured by a camera located outside of the flume. Camera calibration details are given in appendix B.1.

The ‘Plascoat’ particles were approximately $150\ \mu\text{m}$ in diameter, small enough to be considered dynamically unimportant. Although the particles were slightly positively buoyant, their upward settling velocities were small or at least slowly varying compared to their motion beneath the free surface waves (see §3.3). The particles were effectively uniformly mixed throughout the measurement zone, which was achieved by adding new particles between experiments when necessary, mixing up the water column and waiting for the flume to become quiescent before starting experiments. Because of the light sheet, we only tracked a thin slice of particles in the $(x-z)$ -plane. The camera field of view captured half the depth at a time. To obtain a complete distribution with depth, we thus repeated the same experiment twice.

After propagating through the measurement zone, the dispersed wave groups were absorbed by foam wedges within an ‘absorption zone’ located at the downstream end of the wave flume. The measurement zone was located far enough from the wavemaker to minimise the effects of evanescent modes from the wavemaker. To ensure near-quiescent initial conditions for each experiment the flume was allowed to settle for 10 minutes between experiments. Although negligible free surface motions remained after this time period, some slow circulations lingered within the subsurface velocity field; these ‘background particle velocities’ were removed during post-processing of the particle trajectories, as described below. The settling time of 10 minutes was short enough that the slightly positively-buoyant particles remained evenly distributed throughout the water column at the start of each experiment.

3.2. Matrix of experiments

We conducted 12 experiments, as outlined in table 2 with experiment 1 conducted 10 times to determine repeatability. Frequencies were chosen such that the water depth is deep ($k_0 d \gtrsim 3$); amplitudes such that second-order motions are large enough to measure, but not too large so that effects beyond second-order play a role; and the bandwidth parameter $\epsilon = 1/(k_0 \sigma)$ such that the wave group is still quasi-monochromatic (see van den Bremer & Taylor (2016)), but the wave groups not so long that reflections play a role. Having defined ϵ based on length scales in the physical domain and for a Gaussian group, we can obtain an estimate of the number of waves per group of $4\sigma/\lambda_0 = 2/(\pi\epsilon) \approx 2.5 - 4$ (cf. table 2 and figure 9 in appendix A). We investigated both

Experiment	f_0 [Hz]	$\alpha = k_0 a_0$	$\varepsilon = (k_0 \sigma)^{-1}$	$k_0 d$	Phase at focus [deg]	No. of raw trajectories	No. of post-processed trajectories
1	1.25	0.13	0.21	3.16	0	609	115
2	1.25	0.13	0.21	3.16	180	505	92
3	1.25	0.12	0.16	3.16	0	317	53
4	1.25	0.12	0.16	3.16	180	345	51
5	1.25	0.12	0.26	3.16	0	556	107
6	1.25	0.12	0.26	3.16	180	502	130
7	1.5	0.10	0.20	4.53	0	573	147
8	1.5	0.10	0.20	4.53	180	499	87
9	1.5	0.12	0.16	4.53	0	242	56
10	1.5	0.12	0.16	4.53	180	345	90
11	1.5	0.09	0.23	4.53	0	444	99
12	1.5	0.09	0.23	4.53	180	477	119

TABLE 2. Matrix of experiments.

crest-focused (CF) and trough-focused (TF) wave groups, for which frequencies have phases of 0 or π at focus, respectively.

3.3. Data processing and removal of background motion

The recorded images were processed using the Streams software package, a specialist package for flow visualisation applications (Nokes 2014) (see appendix B.2). Lagrangian paths were calculated for particles that had been continuously matched for at least $\pm 6T_g$ with $T_g = \sigma/c_{g,0}$ either side of the time of focus. Despite the settling time between experiments, we found persistent background motion of the particles on a time scale much greater than the linear motion and the motion associated with Stokes drift and the Eulerian return flow beneath the group.

This background motion consists of a combination of upward settling of particles, long waves or ‘seiche modes’ that decay very slowly in the flume and Ekman-type circulation that result from small air flows over the surface that cannot be entirely eliminated in the laboratory. We can estimate the (upward) Stokes settling velocity for our spherical particles as $w = (2/9)((\rho_w - \rho_p)/\rho_w)(gR^2/\nu) = 0.25$ mm/s, where we have used $\rho_p = 0.96$ g/cm³, $\rho_w = 0.98$ g/cm³, $\nu = 1.0 \times 10^{-6}$ m²/s and $R = 75 \times 10^{-6}$ m. We can also estimate the velocity associated with a linear long wave of amplitude $a = 0.1$ mm (probably the smallest that can be detected by the gauges) to be $u = a\sqrt{g/d} = 0.44$ mm/s. For comparison, the Stokes drift near the surface ($z = 0$) and at the point of focus is $u_s = c_{p,0}\alpha^2 = 21$ mm/s for $c_{p,0} = 1.25$ m/s ($f_0 = 1.25$ Hz) and $\alpha = 0.13$ (see table 2). For the same case, the return flow velocity is $u_e = c_{p,0}\alpha^2/(2k_0d - 1/2) = 3.6$ mm/s for $d = 0.5$ m. Fortunately, all these background motions vary more slowly than the waves and their induced mean flows themselves and we can remove these by fitting to the background motion before and after the arrival of the group. The Lagrangian displacements were calculated after removal of this slow background motion, and the quality of the trajectories assessed, resulting in a smaller number of post-processed compared to raw trajectories, as reported in table 2.

When visually assessing the quality of the trajectories, we dismissed particles with incompletely recorded trajectories and particles for which our automatic criterion for identifying the focus time, namely the time at which the horizontal velocity reached a maximum, was not successful. The displacements were calculated between $t = -3T_g$ and $t = +3T_g$, with $t = 0$ corresponding to the focus point, $T_g = \sigma/c_{g,0}$ denoting the group period, and the limits chosen so that the overlying wave group has effectively zero amplitude. The trajectories recorded for

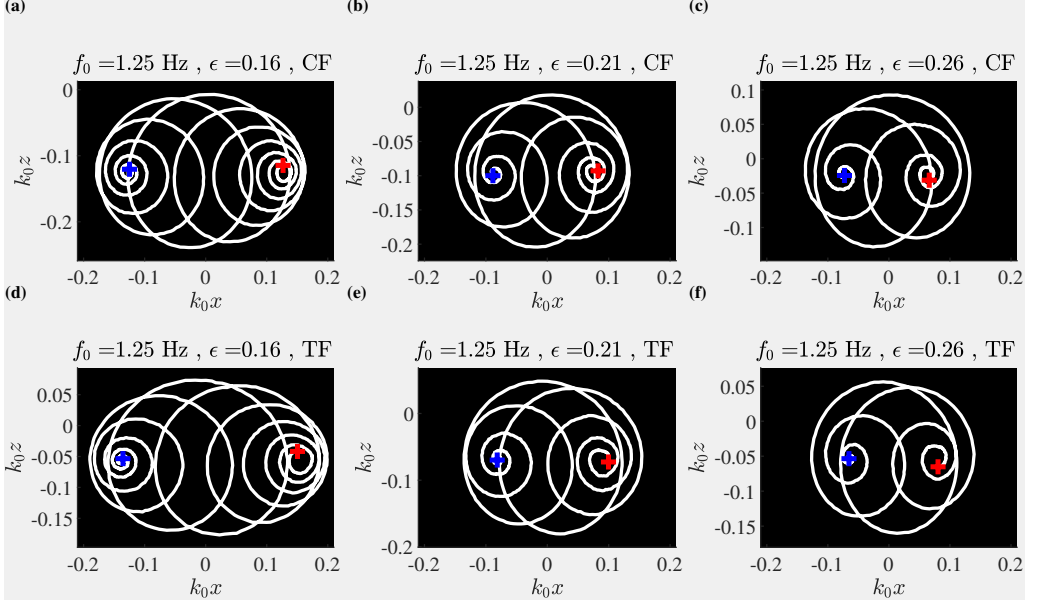


FIGURE 3. Experimental particle trajectories for particles near the surface below crest-focussed (CF, top row) and trough-focussed (TF, bottom row) wave groups for three different groups lengths σ (columns), as denoted by $\epsilon = 1/(k_0\sigma)$. The blue and red + symbols denote experimentally determined initial and final particle positions, respectively.

times outside this window, during which there was no overlying wave group, were then used to fit to and then remove background motion. To do so, we considered four fitting methods and selected the one that minimized the displacement due to the background motion over the window $t = \pm 3T_g$ (see appendix B.3 for further details).

4. Results

4.1. Particle trajectories

Figure 3 shows representative measured particle trajectories near the surface for crest-focussed (CF, top row) and trough-focussed (TF, bottom row) experiments with three different bandwidths (columns). Near the surface, the Stokes drift is dominant, the trajectories for shorter groups (larger ϵ) are made up from fewer orbits with smaller net horizontal displacements, and the vertically-asymmetric relationship between crest-focussed and trough-focussed trajectories is clearest from comparing figures 3c and 3f. The different columns in figure 4 show how particle trajectories vary with depth. Descending in the fluid, the net horizontal displacement transitions from positive near the surface (top row), via zero (middle row) to negative at depth (bottom row). At all depths, the linear wave signature remains present, although the magnitude of the orbits decreases. The horseshoe-shaped mean motion induced by the return flow is evident at depth (fig. 4g-i). In both figures 3 and 4, the blue and red symbols respectively denote the experimentally determined initial and final particle positions, which will be examined for all orbits below.

4.2. Net Lagrangian displacements

After removal of background motion, figure 5 compares net horizontal Lagrangian displacement from experiments (black crosses) to theoretical predictions (red lines) for all experiments. The theoretical predictions are evaluated from (2.5) and (2.7), where we evaluate ω_0 from the

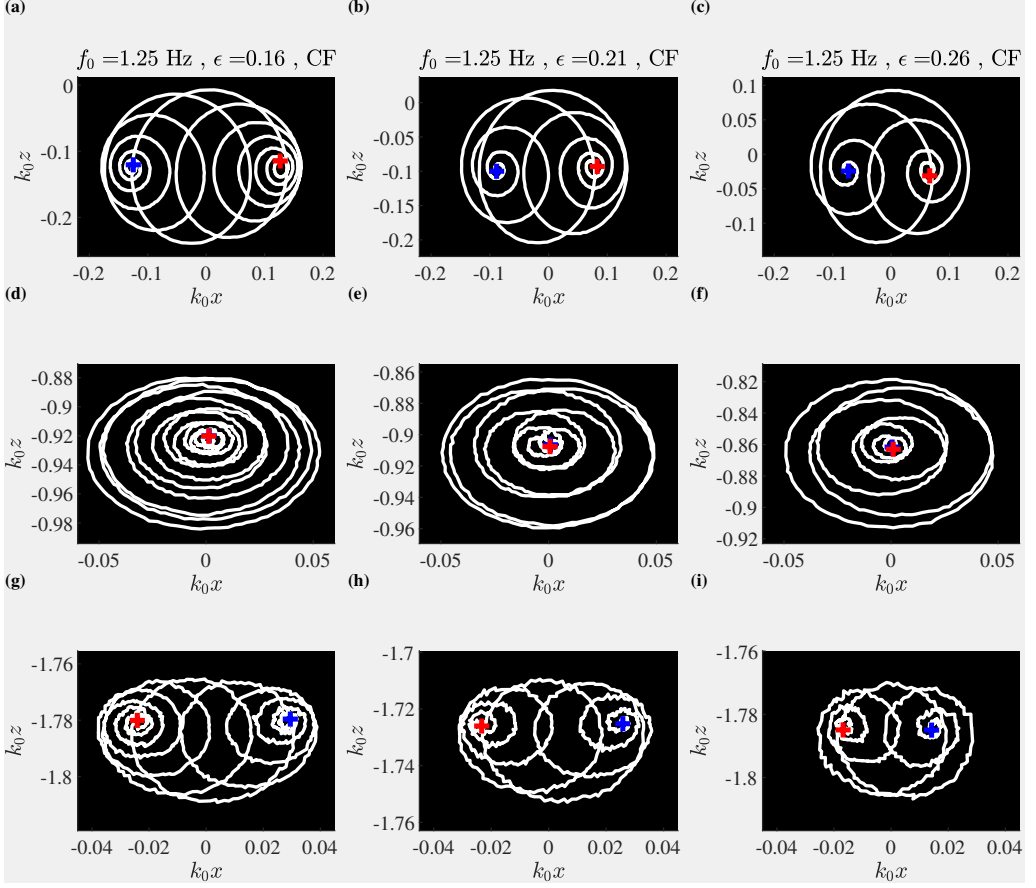


FIGURE 4. Experimental particle trajectories for particles at different depths (rows) for three different group lengths σ (columns), as denoted by $\epsilon = 1/(k_0\sigma)$. The blue and red + symbols denote experimentally determined initial and final particle positions, respectively.

peak of the surface elevation spectrum and compute k_0 from the linear dispersion relationship. Instead of fitting a Gaussian functional form, we numerically evaluate the time integrals in (2.5) and (2.7) over the envelopes extracted from the surface elevation measurements from the gauge, where we first remove bound waves from the spectrum, which has well separated harmonics, using filtering. As expected based on irrotational theory for wave groups, the net positive displacements near the surface dominated by the Stokes drift are accompanied by opposing displacement at depth dominated by the return flow.

The changes in the net displacement due to changes in bandwidth (ϵ) that can be observed in figure 5 are indeed accurately predicted by our leading-order (in ϵ) results (2.5) and (2.7). Keeping k_0 constant, increasing ϵ amounts to a reduction in the group length σ with a consequent reduction in the net displacement, as predicted by (2.5) and (2.7). Although our expressions are only strictly valid in the narrow-banded limit $\epsilon \equiv 1/(k_0\sigma) \rightarrow 0$, higher-order terms only potentially arise at two orders higher in ϵ . Based on the values of ϵ considered here and the calculations performed in van den Bremer & Taylor (2016), we estimate the error associated with our narrow-banded assumption to be a few percent in the worst case.

Using a similar procedure, figure 6 compares the maximum or minimum vertical Lagrangian displacement underneath the centre of the group to their theoretical predictions (2.6) and (2.8). The upward displacement by the Stokes drift near the surface predicted by irrotational theory for

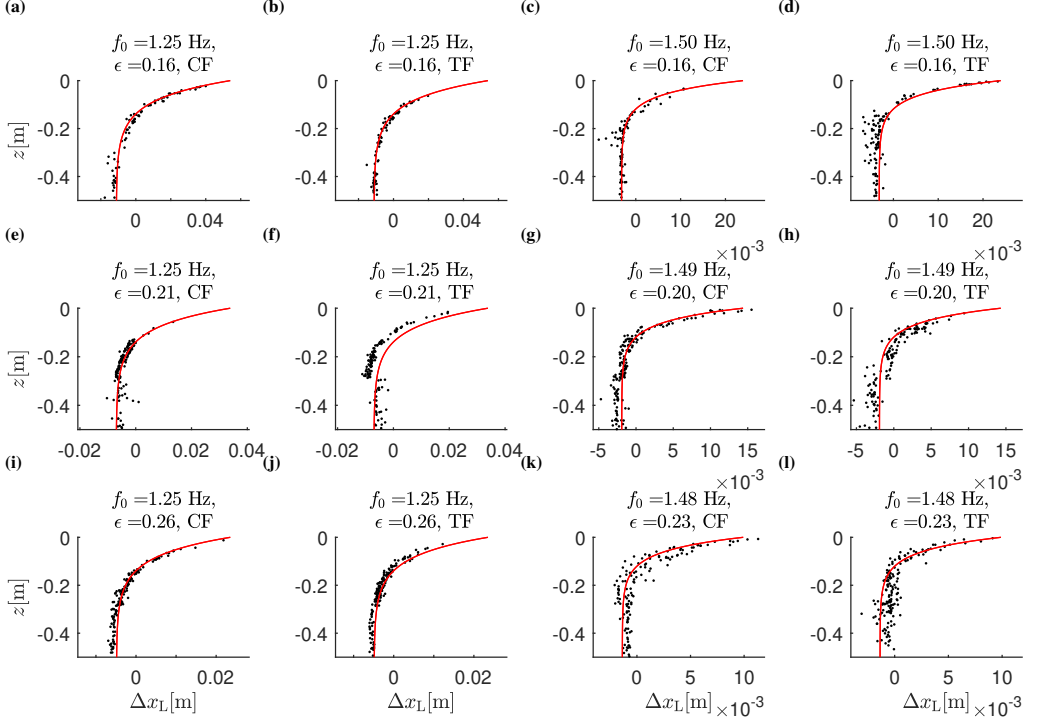


FIGURE 5. Net horizontal Lagrangian displacement from experiments (black dots) compared to theoretical predictions (red lines) for all experiments in table 2.

groups is accompanied by the classical Eulerian set-down at greater depth and decreasing to zero linearly with z to zero at the bottom (cf. (2.8)).

In both figures 5 and 6, the orbits near the surface are not always perfectly captured, which is a result of their larger size and the (reflective) free surface moving through the camera window. Although the scatter in the data is not insignificant for some experiments (addressed in §4.3), they line up well with theoretical predictions, including the magnitude of the displacement by the Stokes drift and the return flow. Finally, figure 7 presents scaled (non-dimensional) Lagrangian displacements from the experiments, noting from (2.5-2.8) that all parameters can be scaled out except for $k_0 d$.

4.3. Repeatability

In order to assess repeatability of experiments and robustness of background motion removal, we conducted experiment 1 ten times. For both the horizontal and the vertical displacements, figure 8 demonstrates good agreement (to within two standard deviations) between experiments and theoretical predictions, notably including the positive vertical displacement by the Stokes drift in figure 8b. Most of the variability for single experiments observed in figures 5-7 is likely due to unpredictable small residual motions present in the flume, which cannot be perfectly removed. In fact, the reason that the agreement with the theoretical solutions appears better for the horizontal displacements (cf. figure 5) than for the vertical displacements (cf. figure 6) is simply that the horizontal displacements are larger, making removal of background motion easier. Furthermore, the displacement associated with longer groups (smaller ϵ) is simply larger and thus easier to measure.

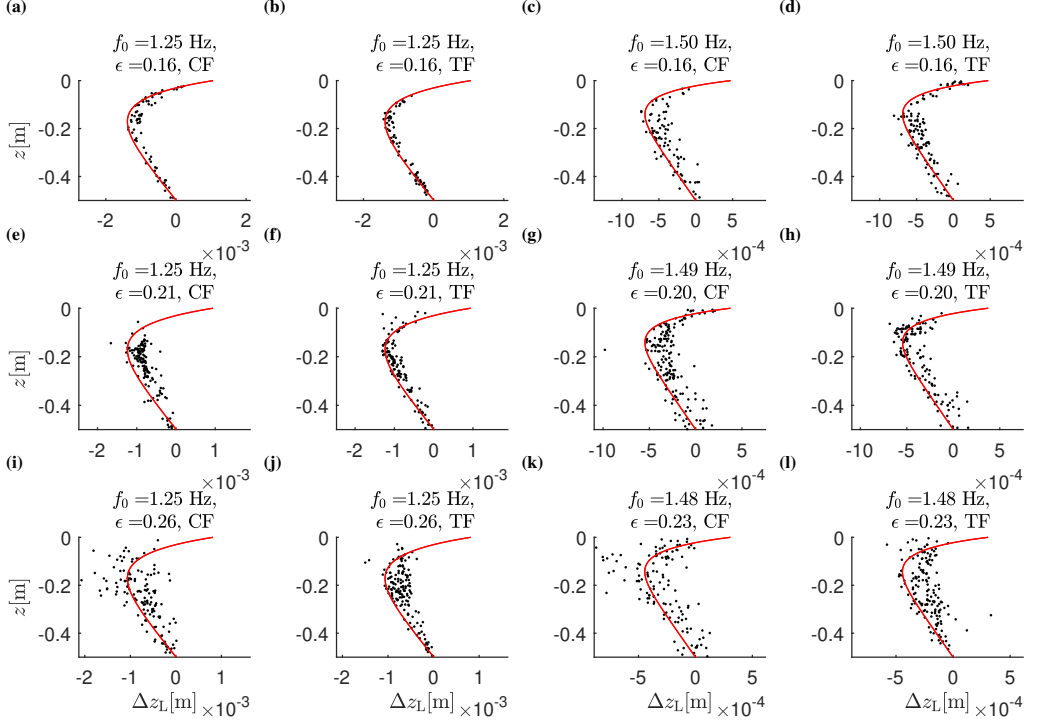


FIGURE 6. Maximum or minimum vertical Lagrangian displacement from experiments (black dots) compared to theoretical predictions (red lines) for all experiments in table 2.

5. Conclusions

This paper has reported on an experimental study of Lagrangian trajectories underneath uni-directional, deep-water surface gravity wave groups and has demonstrated visually their wave-induced Eulerian return flows as well as their Stokes drifts in experiments. Our quasi-monochromatic, small-amplitude, non-breaking experimental observations are in good agreement with leading-order solutions to the irrotational water wave equations. We have also shown that the Stokes drift for groups has both a horizontal and a vertical component, where the former results in a net displacement, whereas the latter leads to a temporary positive set-up for particles a small distance below the centre of a group, defined by a ‘transition’ depth. Such a non-zero vertical Stokes drift is contentious in equations of the Craik & Leibovich (1976)-type (McWilliams 2016; Mellor 2016), but has been predicted to affect Lagrangian buoy records (Herbers & Janssen 2016). For the relatively short, yet still quasi-monochromatic, groups we have examined, boundary layers do not have sufficient time to form and result in streaming of Lagrangian particles. Based on a typical velocity of $a_0\omega_0 = 0.16\text{ m/s}$ for $a_0 = 0.021\text{ m}$ and $\omega_0 = 7.9\text{ rad/s}$ and taking the amplitude a_0 as the typical length scale, we obtain a Reynolds number of 3.5×10^3 (laminar). If we take the group length scale $\sigma = 1.0\text{ m}$ as the characteristic length scale (for $f_0 = 1.25\text{ Hz}$ and $\epsilon = 0.16$), we can estimate the boundary layer thickness that can develop over this scale as $\delta = 4.91 \sqrt{(\sigma\nu)/(a_0\omega_0)} = 0.012\text{ m}$ (Blasius solution for a laminar boundary layer over a plate). This is too small to play a role in our measurements. Furthermore, these short groups avoid the set up of a closed-flume return flow associated with periodic waves, which may transport vorticity, be difficult to control experimentally and could account for some of the confusion in the literature. Although boundary layers, the convection and conduction of vorticity and breaking can probably explain the observed net drift and its depth variation in the

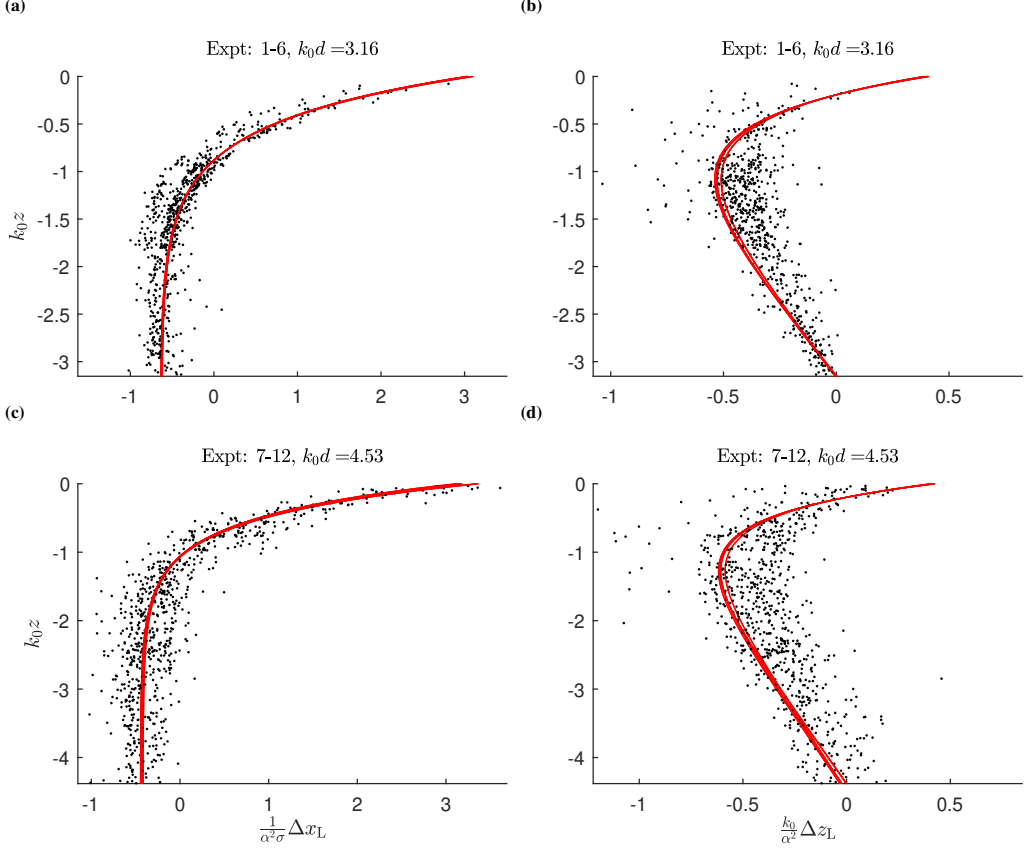


FIGURE 7. Scaled Lagrangian displacement from experiments (black dots) compared to theoretical predictions (red lines): the left column shows net horizontal displacement, the right column maximum or minimum vertical displacement. The rows correspond to $k_0 d = 3.16$ and 4.53 , respectively, where $k_0 d$ is the only non-dimensional parameter that cannot be scaled out. Note that several very slightly different theoretical curves are shown due to small differences between the free surface elevation across experiments that cannot be scaled out.

majority of laboratory experiments, the finding by Smith (2006) of Eulerian counterflows occur that completely cancel the Stokes drift variations at the surface for wave groups in field data is left unexplained.

Although experimental studies, including the present one, have focussed exclusively on particles that behave as perfect Lagrangian tracers, modelling of transport of particles of all sizes and shapes in the upper ocean will require consideration of particle inertia (Eames 2008; Santamaria *et al.* 2013) and anisotropy (DiBenedetto & Ouellette 2018; DiBenedetto *et al.* 2018), as well as ‘surfing’ of particles near the surface (Pizzo 2017; Deike *et al.* 2017). Future work will examine these effects experimentally.

Acknowledgments

TSvdB was supported by a Royal Academy of Engineering Research Fellowship. The authors would like to acknowledge J. Vanneste and C. Higgins for demonstrating that the net displacement (2.7) is not a function z and W. Young for pointing out that there can be a vertical Stokes drift for irrotational water wave groups.

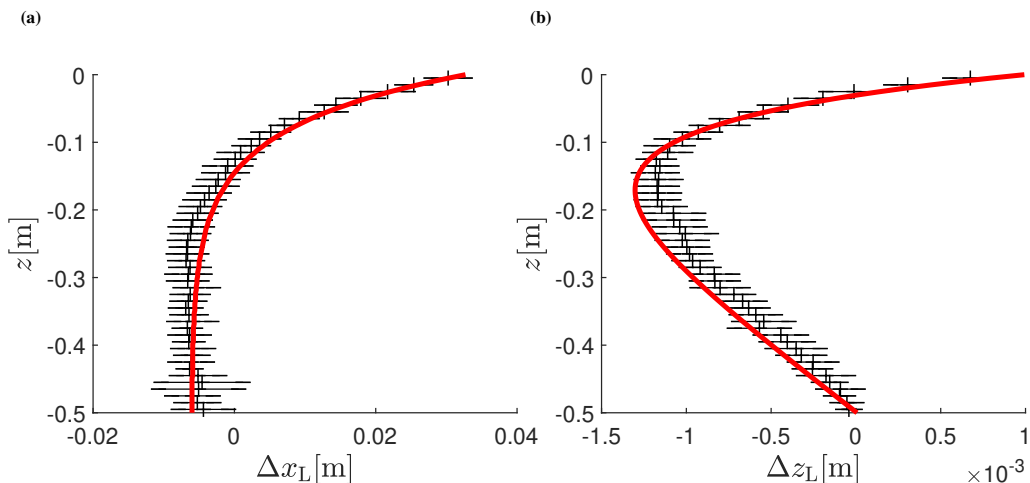


FIGURE 8. Confidence bands on the net horizontal (a) and the maximum or minimum vertical displacement (b) from 10 repeats of experiment 1 with the red lines denoting theoretical predictions. The error bars correspond to two standard deviations either side of the mean.

REFERENCES

- ANDREWS, D. G. & MCINTYRE, M. E. 1978 An exact theory of nonlinear waves on a Lagrangian-mean flow. *J. Fluid Mech.* **89**, 609–646.
- BAGNOLD, R. A. 1947 Sand movement by waves: some small-scale experiments with sand of very low density. *J. Inst. Civil Engng.* **27** (4), 447–469.
- BELCHER, S. E., GRANT, A. L. M., HANLEY, K. E., FOX-KEMPER, B., ROEKEL, L. VAN, SULLIVAN, P. P., LARGE, W. G., ANDY, A. BROWN, HINES, A., CALVERT, D., RUTGERSSON, A., PETERSSON, H., BIDLOT, J. R., JANSSEN, P. A. E. M. & POLTON, J. A. 2012 A global perspective on Langmuir turbulence in the ocean surface boundary layer. *Geophys. Res. Lett.* **39** (18).
- VAN DEN BREMER, T.S. & BREIVIK, Ø. 2017 Stokes drift. *Phil. Trans. R. Soc. Lond. A* **376**, 20170104.
- VAN DEN BREMER, T.S. & TAYLOR, P. H. 2016 Lagrangian transport for two-dimensional deep-water surface gravity wave groups. *Proc. R. Soc. A* **472** (20160159).
- VAN DEN BREMER, T. S. & TAYLOR, P. H. 2015 Estimates of Lagrangian transport by surface gravity wave groups: the effects of finite depth and directionality. *J. Geophys. Res.* **120** (4), 2701–2722.
- BÜHLER, O. 2014 *Waves and Mean Flows*, 2nd edn. Cambridge University Press, Cambridge, UK.
- CHRISTENSEN, K. H. & TERRILE, E. 2009 Drift and deformation of oil slicks due to surface waves. *J. Fluid Mech.* **620**, 313–332.
- CRAIK, A. D. D. & LEIBOVICH, S. 1976 A rational model for Langmuir circulations. *J. Fluid Mech.* **73** (3), 401–426.
- D’ASARO, E. A., THOMSON, J., SHCHERBINA, A. Y., HARCOURT, R. R., CRONIN, M. F., HEMER, M. A. & FOX-KEMPER, B. 2014 Quantifying upper ocean turbulence driven by surface waves. *Geophys. Res. Lett.* **41** (1), 102–107.
- DEIKE, L., PIZZO, N. & MELVILLE, W. K. 2017 Lagrangian transport by breaking surface waves. *J. Fluid Mech.* **829**, 364–391.
- DIBENEDETTO, M. H. & OUELLETTE, N. T. 2018 Preferential orientation of spheroidal particles in wavy flow. *J. Fluid Mech.* **856**, 850–869.
- DIBENEDETTO, M. H., OUELLETTE, N. T. & KOSEFF, J. R. 2018 Transport of anisotropic particles under waves. *J. Fluid Mech.* **837**, 320–340.
- DRIVDAL, M., G. BROSTRÖM, G. & CHRISTENSEN, K. H. 2014 Wave-induced mixing and transport of buoyant particles: application to the Statfjord A oil spill. *Ocean Science* **10** (6), 977–991.
- VAN DYKE, M. 1982 *An album of fluid motion*. Stanford, USA: The Parabolic Press.
- EAMES, I. 2008 Settling of particles beneath water waves. *J. Phys. Oceanogr.* **38**, 2846–2853.
- GROENEWEG, J. & KLOPMAN, G. 1998 Changes of the mean velocity profiles in the combined wave-current motion described in a GLM formulation. *J. Fluid Mech.* **370**, 271–269.

- GRUE, JOHN & KOLAAS, JOSTEIN 2017 Experimental particle paths and drift velocity in steep waves at finite water depth. *J. Fluid Mech.* **810**, R1.
- HANEY, S., FOX-KEMPER, B., JULIEN, K. & WEBB, A. 2015 Symmetric and geostrophic instabilities in the wave-forced ocean mixed layer. *J. Phys. Oceanogr.* **45** (12), 3033–3056.
- HERBERS, T. H. C. & JANSSEN, T. T. 2016 Lagrangian surface wave motion and Stokes drift fluctuations. *J. Phys. Oceanogr.* **46** (4), 1009–1021.
- JONES, C. E., DAGESTAD, K., BREIVIK, Ø., HOLT, B., RÖHRSHRS, J., CHRISTENSEN, K., ESPESETH, M., BREKKE, C. & SKRUNES, S. 2016 Measurement and modelling of oil slick transport. *J. Geophys. Res.* **121** (10), 7759–7775.
- LEBRETON, L., SLAT, B., FERRARI, F., SAINTE-ROSE, B., AITKEN, J., MARTHUSE, R., HAJBANE, S., CUNSOLO, S., SCHWARZ, A., LEVIVIER, A., NOBLE, K., DEBELIAK, P., MARAL, H., SCHOENEICH-ARGENT, R., BRAMBINI, R. & REISSER, J. 2018 Evidence that the Great Pacific Garbage Patch is rapidly accumulating plastic. *Scientific Reports* **8**, 4666.
- LONGUET-HIGGINS, M.S. 1953 Mass transport in water waves. *Phil. Trans. R. Soc. Lond. A* **245**, 535–581.
- LONGUET-HIGGINS, M.S. & STEWART, R.W. 1962 Radiation stress and mass transport in gravity waves, with applications to ‘surf beats’. *J. Fluid Mech.* **13**, 481–504.
- LONGUET-HIGGINS, M.S. & STEWART, R.W. 1964 Radiation stresses in water waves; a physical discussion, with applications. *Deep-Sea Res.* **2**, 529–562.
- MCALLISTER, M. L., ADCOCK, T. A. A., TAYLOR, P. H. & VAN DEN BREMER, T. S. 2018 The set-down and set-up of directionally spread and crossing surface gravity wave groups. *J. Fluid Mech.* **835**, 131–169.
- MCINTYRE, M. E. 1981 On the wave momentum myth. *J. Fluid Mech.* **106**, 331–347.
- MCINTYRE, M. E. 1988 A note on the divergence effect and the Lagrangian-mean surface elevation in periodic water waves. *J. Fluid Mech.* **189**, 235–242.
- MCWILLIAMS, J. C. 2016 Submesoscale currents in the ocean. *Proc. R. Soc. Lond. A* **472**, 2189.
- MCWILLIAMS, J. C. & RESTREPO, J.M. 1999 The wave-driven ocean circulation. *J. Phys. Oceanogr.* **29**, 2523–2540.
- MCWILLIAMS, J. N., RESTREPO, J. M. & LANE, E. M. 2004 An asymptotic theory for the interaction of waves and currents in coastal waters. *J. Fluid Mech.* **511**, 135–178.
- MEI, C. C., LIU, P. L. F. & CARTER, T. G. 1972 Mass transport in water waves. *Tech. Rep.* 146. MIT Rep. Ralph M. Parsons Lab. Water Resources Hydrodynamics.
- MELLOR, G. 2016 On theories dealing with the interaction of surface waves and ocean circulation. *J. Geophys. Res. Oceans* **121**, 4474–4486.
- MELVILLE, W. K. & RAPP, R. 1988 The surface velocity field in steep and breaking waves. *J. Fluid Mech.* **189**, 1–22.
- MONISMITH, S. G., COWEN, E.A., NEPF, H. M., MAGNAUDET, J. & THAIS, L. 2007 Laboratory observations of mean flows under surface gravity waves. *J. Fluid Mech.* **573**, 131–147.
- NOKES, R. 2014 *Streams 2.02: System theory and design*. Canterbury, New Zealand: University of Canterbury.
- PAPROTA, M., SULISZ, W. & REDA, A. 2016 Experimental study of wave-induced mass transport. *J. Hydraul. Res.* **54** (4), 423–434.
- PIZZO, N. & MELVILLE, W. 2013 Vortex generation by deep-water breaking waves. *J. Fluid. Mech.* **734** (198–218).
- PIZZO, N. E. 2017 Surfing surface gravity waves. *J. Fluid Mech.* **823**, 316–328.
- RÖHR, J., CHRISTENSEN, K. H., HOLE, L. R., BROSTRÖM, G., DRIVDAL, M. & SUNDBY, S. 2012 Observation-based evaluation of surface wave effects on currents and trajectory forecasts. *Ocean Dynam.* **62** (10), 1519–1533.
- SANTAMARIA, F., BOFFETTA, F., MARTINS AFONSO, M., MAZZINO, A., ONORATO, M. & PUGLIESE, D. 2013 Stokes drift for inertial particles transported by water waves. *Europhys. Lett.* **102** (1), 14003.
- SCHÄFFER, H. A. 1996 Second-order wavemaker theory for irregular waves. *Ocean Eng.* **23**, 47–88.
- SMITH, J. A. 2006 Observed variability of ocean wave Stokes drift, and the Eulerian response to passing groups. *J. Phys. Oceanogr.* **36**, 1381–1402.
- STOKES, G. G. 1847 On the theory of oscillatory waves. *Trans. Camb. Philos. Soc.* **8**, 441–455.
- SULLIVAN, P. P. & MCWILLIAMS, J. C. 2010 Dynamics of winds and currents coupled to surface waves. *Annu. Rev. Fluid Mech.* **42**, 19–42.
- SWAN, C. 1990 Convection within an experimental wave flume. *J. Hydraul. Res.* **28**, 273–282.

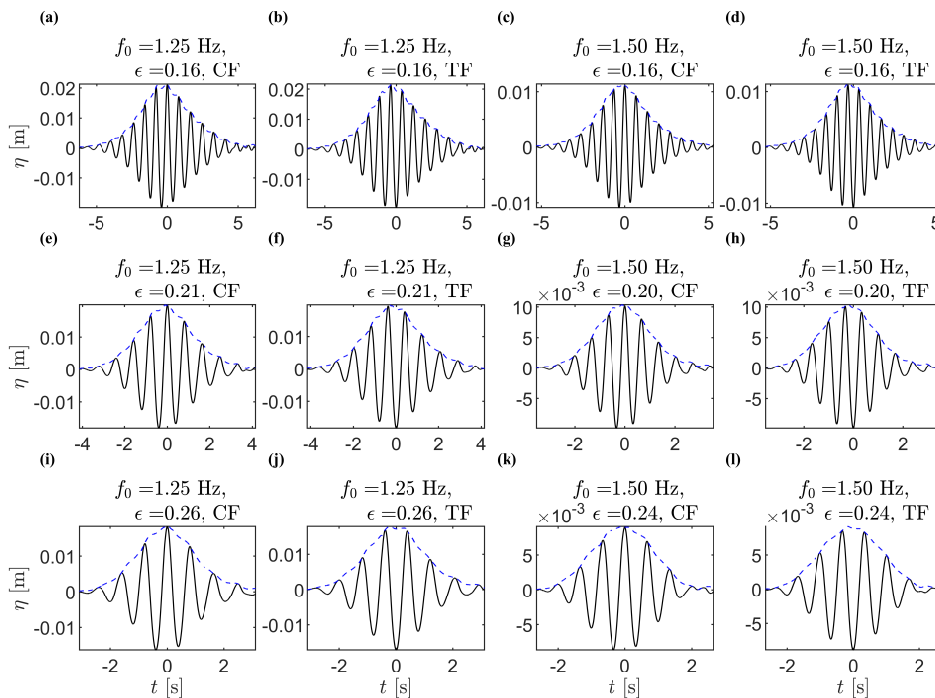


FIGURE 9. Measured free surface elevation signals for the 12 experiments in table 2: the blue lines dashed denote the envelopes obtained using a Hilbert transform.

SWAN, C. & SLEATH, J. F. A. 1990 A second approximation to the time-mean Lagrangian drift beneath progressive gravity waves. *Ocean Eng.* **1**, 65–79.

TRINANES, J. A., OLASCOAGA, M. J., GONI, G. J., MAXIMENKO, N. A., GRIFFIN, D. A. & HAFNER, J. 2016 Analysis of flight MH370 potential debris trajectories using ocean observations and numerical model results. *J. Oper. Oceanogr.* **9** (2), 126–138.

UMEYAMA, M. 2012 Eulerian-Lagrangian analysis for particle velocities and trajectories in a pure wave motion using particle image velocimetry. *Philos. T. Roy. Soc. A* **370** (1687), 1687–1702.

WEBER, J. E. H. 2011 Do we observe Gerstner waves in wave tank experiments? *Wave Motion* **48** (4), 301–309.

WHITTAKER, C.N., FITZGERALD, C.J., RABY, A.C., TAYLOR, P.H., ORSZAGHOVA, J. & BORTHWICK, A.G.L. 2017 Optimisation of focused wave group runup on a plane beach. *Coast. Eng.* **121**, 44–55.

Appendix A. Measured free surface elevation signals

Figure 9 shows the unfiltered measured free surface elevation signals for the 12 experiments in table 2.

Appendix B. Experimental procedure and data processing

B.1. Camera settings and calibration

During the experiments, a light-emitting diode (LED) light box located above the flume illuminated a two-dimensional plane approximately 1 m long and 10 mm thick. Ambient lighting was removed during these experiments, to maximise the contrast between the illuminated particles and the image background. A Photron SA4 high-speed camera captured the particle motions

within the plane illuminated by the LED light box. Each experiment was repeated multiple times to ensure complete coverage of the depth and some overlap between different camera windows as a result. The camera captured images at 125 frames/s, with a resolution of 1024 by 1024 pixels and a shutter speed of $1/125$ s (i.e. opening the shutter for the duration of image acquisition). This shutter speed achieved an acceptable compromise between the requirements of obtaining very sharp images (requiring a high shutter speed) and allowing sufficient light to enter the CCD of the camera during each image (requiring a low shutter speed). Before conducting each experiment, the camera captured a calibration image of a ruler, allowing quantification of the pixel scale and any distortion in the images (barrel-pincushion distortions were found to be negligible for these tests). The image was calibrated by placing a ruler in the light sheet.

B.2. Image processing and particle tracking

The particles within each image were identified using a dual threshold algorithm, which first searched the image for pixels with an intensity greater than a particular threshold, identified the maximum pixel intensity within the group of pixels and finally defined the particle boundaries based on a fraction of this maximum intensity. This algorithm has the advantage of correctly identifying stationary and moving particles within a range of lighting conditions. The identified particles were subsequently matched between frames using an ‘auction’ optimisation algorithm. This auction algorithm optimised the particle matches by minimising the total cost of all potential matches for each successive pair of frames, where the cost was first assigned based on particle distance, then based on the (matched) particle velocities in a small region. The velocities of matched particles were finally used to generate additional matches where appropriate.

B.3. Removal of background motion

In order to remove background motion, we first centre the signal around the time of focus, chosen as the time of the maximum horizontal velocity, so that it corresponds to $t = 0$ and then consider four ways of fitting to the background motion in the signals $(x(t), z(t))$:

(i) linear fit to the x -displacement prior to wave group arrival over $(-6T_g, -3T_g)$ and quadratic fit to the z -displacement before and after wave group arrival over $(-6T_g, -3T_g)$ and $(3T_g, 6T_g)$;

(ii) linear fit to the x -displacement prior to wave group arrival over $(-9T_g, -3T_g)$ and quadratic fit to the z -displacement before and after wave group arrival over $(-9T_g, -3T_g)$ and $(3T_g, 9T_g)$;

(iii) linear fit to the x -displacement prior to wave group arrival over $(-12T_g, -3T_g)$ and quadratic fit to the z -displacement before and after wave group arrival over $(-12T_g, -3T_g)$ and $(3T_g, 12T_g)$;

(iv) linear fit to the x -displacement and quadratic fit to the z -displacement before and after wave group arrival over $(-9T_g, -3T_g)$ and $(3T_g, 9T_g)$;

where we estimated the group velocity $c_{g,0}$ and hence the group period T_g from the spectral peak of the measured free surface time series.

All trajectories were visually inspected to ensure the orbit was complete and the focus location correctly identified. Of the four fitting methods, we selected the method that minimised the net ‘background’ displacement of the particle within the fit windows for each trajectory. After satisfactory processing of the particle orbits, the net displacements were calculated between $-3T_g$ and $3T_g$.